A boundary integral method for modelling vibroacoustic energy distributions in uncertain built up structures

Janis Bajars, David J. Chappell *

Nottingham Trent University, School of Science and Technology, Clifton Campus, Clifton Lane, Nottingham, NG11 8NS, UK

A B S T R A C T

A phase-space boundary integral method is developed for modelling stochastic high-frequency acoustic and vibrational energy transport in both single and multi-domain problems. The numerical implementation is carried out using the collocation method in both the position and momentum phase-space variables. One of the major developments of this work is the systematic convergence study, which demonstrates that the proposed numerical schemes exhibit convergence rates that could be expected from theoretical estimates under the right conditions. For the discretisation with respect to the momentum variable, we employ spectrally convergent basis approximations using both Legendre polynomials and Gaussian radial basis functions. The former have the advantage of being simpler to apply in general without the need for preconditioning techniques. The Gaussian basis is introduced with the aim of achieving more efficient computations in the weak noise case with near-deterministic dynamics. Numerical results for a series of coupled domain problems are presented, and demonstrate the potential for future applications to larger scale problems from industry.

1. Introduction

Noise and vibration simulations for mechanical structures are commonly performed using numerical solvers for linear wave equations [1,2]. The underlying numerical technologies are typically based on finite element methods, finite volume methods, boundary element methods or a variety of spectral methods. There are, however, two fundamental limitations when numerically approximating the solutions of wave equations directly in this manner. Firstly, the size of the numerical models required to obtain reliable results will eventually grow large enough to become computationally prohibitive when the local wavelengths become significantly smaller than the dimensions of the physical system. Secondly, the modal density increases with the frequency and, as a consequence, the vibrational responses of "identical" manufactured structures from the same production line can differ greatly in the high frequency regime. That is, uncertainties play a more important role when the structural modes become sufficiently dense that they can exchange positions due to small structural differences within standard manufacturing tolerances. For these reasons statistical methods for predicting averaged energy distributions, such as Statistical Energy Analysis (SEA) [3], have become popular tools for high frequency noise and vibration simulations [4]. However, the underlying assumptions of SEA are often hard to verify *a-priori*, and the method only provides a coarse description of the structure under consideration since constant energy levels are assumed throughout relatively large substructures of the overall model [5].

---

* Corresponding author.
  E-mail addresses: janis.bajars@ntu.ac.uk (J. Bajars), david.chappell@ntu.ac.uk (D.J. Chappell).

An alternative framework that can provide a more detailed description of the vibrational or acoustic energy distribution is to model wave energy transport at high frequencies via a geometrical ray description, which neglects interference and other wave effects. The underlying wave problem is then reduced to tracking densities of rays or particles in phase-space and becomes part of a wider class of mass, particle or energy transport problems driven by an underlying deterministic velocity field. The computational cost of direct ray or beam tracing methods, based on following rays or beams from a source to a receiver, scales with the number of paths that must be modelled. For complex domains including many reflections, the number of paths can grow so rapidly that applications in room acoustics are typically limited to including at most second order reflections [6]. Furthermore, in complex structures there may additionally be mode conversion and refraction effects to take into account. In these circumstances, indirect methods based on conservation laws such as the Liouville equation can provide a more practical alternative by propagating ray densities (instead of the rays themselves) through phase-space [7–10]. The deterministic propagation of ray densities according to the Liouville equation can be expressed using a transfer operator, known as the Frobenius–Perron operator [11], which transports ray densities along the trajectories of a dynamical system in general (in our case a Hamiltonian ray flow). These ideas have also found their way into the literature in computer graphics [12] and room acoustics [13] amongst others, where the corresponding transfer operator equation is often labelled the rendering equation.

A variety of techniques have been proposed for the discretisation of the Frobenius–Perron operator, with the aim of developing efficient numerical tools for practical applications. Domain based transfer operator approaches involve subdividing the phase-space and approximating the transition rates between these subdivided regions. One of the simplest approaches of this type is known as the Ulam method [14]. For a discussion of convergence properties of the Ulam method in one and several dimensions, see Refs. [15] and [16], respectively. One shortcoming of the Ulam method is that it typically only exhibits sub-linear convergence rates. As a result of this slow convergence and the high-dimensionality of the phase-space, these methods have typically found only limited applications. In order to reduce memory costs and/or speed up the convergence, both wavelet and spectral methods have been proposed [17,18]. A boundary integral reformulation of the Frobenius–Perron operator for a ray flow is derived in Ref. [10], which can be used to determine the stationary ray density (in the long-time limit) corresponding to the high-frequency asymptotic solution of a frequency-domain wave problem. This has the advantage of reducing the dimensionality from a full phase-space model to the Birkhoff coordinates for the phase-space on the boundary.

In this work we consider the ray dynamical modelling of wave energy transport through uncertain structures, which leads instead to a stochastic velocity field driving the energy transport. We propagate ray densities using the corresponding conservation law, here provided by the Fokker–Planck equation for the stochastic evolution of ray densities in phase-space under the action of a noisy flow [11,19]. Direct treatment of the Fokker–Planck equation is often considered infeasible [20], and in this work we will apply a boundary integral formulation of the Fokker–Planck equation for a Hamiltonian flow, where the associated boundary integral operator will take the form of a stochastic evolution operator. Through this approach we achieve a reduction in dimensionality to the boundary phase-space, which makes the corresponding numerical models both smaller and simpler to implement. Stochastic evolution operators have been extensively studied over the last twenty years via periodic orbit techniques [21–25]. Initial work focused on determining spectral properties of the Fokker–Planck operator for Langevin flows in the weak noise limit. However, more recent work has considered higher dimensional cases [26] and the estimation of stationary distributions [27]. Modified Ulam-type methods have also been devised for stochastic transfer operators, see for example Refs. [28,29].

The approach taken here will be based on a modification of a recently-proposed boundary integral reformulation of a stochastic evolution operator, for the case when the noisy flow has been replaced by a noisy boundary map [30]. The resulting boundary integral operator is described in Sect. 2. The modified formulation proposed here has the advantage that it can be generalised from single to multi-domain problems by restricting the range of the noisy boundary map to the edge where the corresponding deterministic map arrives; see Sect. 2.3 for further details. In general, the spatial domain is relatively complex (including corners) compared to the momentum domain, which simply corresponds to the range of angles pointing into the spatial domain at any given boundary point. Note also that highly peaked solutions with respect to the momentum variable are commonplace in ray tracing problems, whereas the solutions typically exhibit a milder dependence on the spatial variable. A local and low order approximation scheme in the spatial variable using piecewise constant collocation is therefore appropriate and furthermore, leads to simplifications in the implementation of the boundary integrals as detailed in Sect. 3.1. For the approximation with respect to the momentum variable we consider two different possibilities for a spectral collocation method in Sect. 3.2; a well-conditioned basis approximation using Legendre polynomials and a radial basis approximation using Gaussian functions. Despite requiring additional preconditioning strategies in order to obtain convergence, the latter has the advantage of providing an exact representation of the typical initial conditions in our proposed model and has the potential for computational cost savings in the case of near-deterministic propagation. These phase-space collocation schemes are detailed throughout Sect. 3 and have the advantage that we can demonstrate the consistency of our numerical implementation with theoretical convergence results for second-kind integral equations with bounded operators [31], as discussed in Sect. 4. We note that these results do not carry over to the Nyström method based discretisation applied in Ref. [30]. Finally, we detail a series of numerical experiments for multi-domain problems in Sect. 5, demonstrating the potential of the proposed methods to model built up structures from industrial applications in high-frequency structural vibrations and acoustics.

2. Stochastic propagation of phase-space densities: a boundary integral approach

In this section we describe a boundary integral model for the stochastic propagation of phase-space densities in both single and multi-domain problems.

2.1. Governing boundary integral equations

Consider phase-space in two-dimensions with position vector $\mathbf{r} \in \mathbb{R}^2$ and momentum (or slowness) vector $\mathbf{p} \in \mathbb{R}^2$. Let $\Omega \subset \mathbb{R}^2$ denote a finite domain with an associated speed of propagation c. The Hamiltonian $\hat{H} = c|\mathbf{p}| = 1$ describes the ray trajectories within Ω between reflections at the boundary $\Gamma = \partial\Omega$ [8]. Note that this Hamiltonian can be applied directly for ray tracing approximations of acoustic waves and in-plane wave modes in plates; modifications are necessary for modelling flexural plate motion since the associated dispersion relation changes from linear to quadratic in $|\mathbf{p}|$ [32]. The stochastic propagation of a density g through phase-space is described by an operator of the form

$$\mathcal{L}_{\boldsymbol{\sigma}} g(X) = \int_Q f_{\boldsymbol{\sigma}}(X - \varphi(Y))g(Y)\,\mathrm{d}Y. \tag{1}$$

Here $Q = \Gamma \times (-c^{-1}, c^{-1})$ denotes the phase-space on the boundary and the corresponding coordinates $X \in Q$ are written in the form $X = (s, p)$, where s is an arc-length parametrisation of Γ and $p = c^{-1}\sin(\theta)$ is the tangential component of the momentum vector $\mathbf{p}$ at the point s. The angle $\theta \in (-\pi/2, \pi/2)$ is formed between the trajectory leaving the boundary at s and the normal vector to Γ (also at s). The deterministic boundary map $\varphi : Q \to Q$ maps a vector $Y = (t, q) \in Q$ to $\varphi(Y) \in Q$, and corresponds to the composition of a translation in the spatial coordinate and a rotation to the direction corresponding to a specular reflection. The kernel of the boundary integral operator (1) is given by a probability density function (PDF) $f_{\boldsymbol{\sigma}}$ such that

$$\int_Q f_{\boldsymbol{\sigma}}(X - \varphi(Y))\,\mathrm{d}Y = 1, \tag{2}$$

for all $X \in Q$ and $\boldsymbol{\sigma}$ is a parameter set controlling its shape.

With reference to applications in vibroacoustics, this probabilistic behaviour could be attributed to, for example, uncertain fluctuations in the propagation speed c, roughness of the reflecting boundary or uncertainties in the boundary conditions/source terms. Note that in contrast to the models considered in [21,24], the range of integration in the domains considered here is in general bounded, which has implications for the choice of suitable PDFs $f_{\boldsymbol{\sigma}}$ as discussed in the next section. For simplicity, we will also restrict to convex domains Ω to avoid complications related to the incorporation of visibility functions.

For an initial boundary density ρ_0 on Q, the final stationary density distribution ρ including contributions from arbitrarily many reflections may be computed using the following boundary integral equation (see for example [30,9])

$$(I - \mathcal{L}_{\boldsymbol{\sigma}})\rho = \rho_0. \tag{3}$$

The invertibility of the operator $(I - \mathcal{L}_{\boldsymbol{\sigma}})$, as well as bounds on the norm of the inverse, may be established using a Neumann series argument as discussed in Appendix A. Equation (3) is, in fact, derived from the series

$$\rho = \sum_{j=0}^{\infty} (\mathcal{L}_{\boldsymbol{\sigma}})^{(j)} \rho_0, \tag{4}$$

where the superscript (j) denotes that we apply the operator $\mathcal{L}_{\boldsymbol{\sigma}}$ j times. For the sum (4) to converge, energy losses must be introduced into the system, which could take place at the boundaries, or along the trajectories. In this work we apply viscous damping, which is a standard damping model for vibration problems and corresponds to friction with the surrounding gas or fluid. For acoustic problems, simpler boundary absorption type conditions are more common. The damping is incorporated by introducing a weight factor $w(X, Y)$, including a dissipative term, inside the integral in the definition of $\mathcal{L}_{\boldsymbol{\sigma}}$. For viscous damping we apply a factor of the form $\exp(-\mu d(s, t))$, where $\mu \geq 0$ is the (viscous) damping parameter and $d(s, t)$ denotes the Euclidean distance between the boundary points s and t. The damping factor therefore introduces a dependence on the trajectory length and the density ρ decays exponentially along this length with decay rate μ. For the extension to coupled convex domains connected along a common interface, then $w(X, Y)$ will also contain reflection/transmission probabilities at the interface.

Once the final boundary density ρ (from summing infinitely many iterates of $\mathcal{L}_{\boldsymbol{\sigma}}$) has been found using equation (3), the stationary interior density ρ_Ω is calculated via (see [10] for further details)

$$\rho_\Omega(\mathbf{r}) = \frac{1}{c^2} \int_\Gamma \rho(s, p) \frac{\cos(\vartheta(s, \mathbf{r}))}{|\mathbf{r} - \mathbf{r}_s|} e^{-\mu|\mathbf{r} - \mathbf{r}_s|}\,\mathrm{d}s, \tag{5}$$
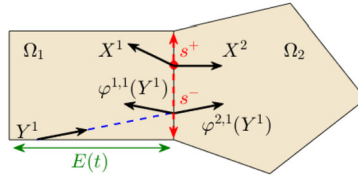
Fig. 1. Tracking ray trajectories in a multi-domain problem via a boundary map with added noise (s_ϵ, p_ϵ), where s_ϵ has infimum/supremum given by $s^\pm$.

where $\mathbf{r} \in \Omega$ is a prescribed solution point and $\mathbf{r}_s$ denotes the Cartesian coordinates of the point $s \in \Gamma$. The angle $\vartheta(s, \mathbf{r})$ is formed between the normal vector to Γ at s and the direction vector pointing towards the point $\mathbf{r}$ from the point $s \in \Gamma$.

2.2. On the choice of probability density function f_σ

We may interpret the evolution given by the operator in equation (1) as originating from a stochastic boundary map φ_σ with added noise, that is,

$$\varphi_\sigma(Y) = X$$
$$= \varphi(Y) + X_\varepsilon, \tag{6}$$

where $X_\varepsilon = (s_\varepsilon, p_\varepsilon)$ are random variables drawn from the PDF f_σ. For $X \in Q$ given, we enforce that $\varphi(Y) = X - X_\varepsilon$ is in the range of the deterministic map φ. We express $\varphi = (\varphi_s, \varphi_p)$ in terms of its position and momentum components and again write the initial coordinate as $Y = (t, q)$. For a single domain, the range of $\varphi_s(Y)$ consists of all points on Γ except those on the edge $E(t)$ containing the point t and $\varphi_p(Y) \in (-c^{-1}, c^{-1})$, see Fig. 1. We therefore restrict the ranges from which X_ε are sampled to ensure $\varphi(Y) \in (\Gamma \setminus E(t)) \times (-c^{-1}, c^{-1})$ in equation (6). In fact, the support of the PDF in the spatial variable shown in Fig. 1 will be restricted to the target edge of the stochastic boundary map φ_σ in order to facilitate a direct extension to problems on built up domains as described in Sect. 2.3.

Denoting the finite support of the PDF by (X^-, X^+), where $X^\pm = (s^\pm, p^\pm)$, we note that $X^\pm$ depends on the arrival coordinate X as detailed in Ref. [30], but the explicit dependence is suppressed in the notation here for brevity. In this work, the support of the PDF in the spatial variable is restricted to the target edge and hence one difference from the model presented in Ref. [30] is that there is no longer any dependence of $s^\pm$ on the initial edge $E(t)$. We will base our model on a truncated normal distribution and define the corresponding PDF to be

$$f_\sigma(X_\varepsilon; X^-, X^+) = f_{\sigma_1}(s_\varepsilon; s^-, s^+) \, f_{\sigma_2}(p_\varepsilon; p^-, p^+),$$
$$:= \left(\frac{\chi(s_\epsilon; s^-, s^+) \exp\left(-\frac{s_\varepsilon^2}{2\sigma_1^2}\right)}{\sqrt{2\pi}\,\sigma_1 \psi_{\sigma_1}(s^-, s^+)} \right) \left(\frac{\chi(p_\epsilon; p^-, p^+) \exp\left(-\frac{p_\varepsilon^2}{2\sigma_2^2}\right)}{\sqrt{2\pi}\,\sigma_2 \psi_{\sigma_2}(p^-, p^+)} \right), \tag{7}$$

where $\sigma = (\sigma_1, \sigma_2)$ represents the standard deviation of the underlying bivariate and uncorrelated normal distribution with mean $\mathbf{0} = (0, 0)$. Note that χ is simply a cut-off function for restricting f_σ to (X^-, X^+) as follows

$$\chi(s_\varepsilon; s^-, s^+) = H(s^+ - s_\varepsilon) - H(s^- - s_\varepsilon),$$

where H is the Heaviside step function. A normalisation to ensure the conservation of probability (2) is defined through the functions ψ_{σ_1} and ψ_{σ_2}, and is given by

$$\psi_{\sigma_1}(s^-, s^+) = \frac{1}{2}\left(\text{erf}\left(\frac{s^+}{\sqrt{2}\sigma_1}\right) - \text{erf}\left(\frac{s^-}{\sqrt{2}\sigma_1}\right) \right), \tag{8}$$

where ψ_{σ_2} is defined analogously.

The choice of PDF (7) offers greater flexibility in terms of uncertainty modelling compared with an SEA-type model, which corresponds to a simple uniform distribution [30], as well as having a number of favourable properties. In particular, taking the limit as $\sigma \to 0$, then the distribution becomes increasingly sharp and the PDF (7) tends to a two-dimensional delta distribution localised around $X_\varepsilon = X - \varphi(Y) = \mathbf{0}$, which leads to a deterministic model. On the other hand, as σ_1 and σ_2 tend to ∞ then the PDF (7) simplifies to the uniform distribution. Therefore a stochastic propagation model based on the PDF (7) can capture both the near deterministic case for small σ, as well as increasingly random propagation as the parameters σ are increased. The application of this framework for modelling uncertain fluctuations in the propagation speed c, roughness of the reflecting boundary and uncertainties in the boundary conditions or source terms has been discussed in Ref. [33].
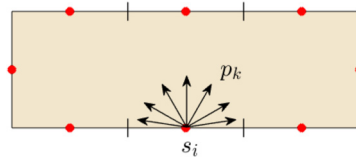
Fig. 2. An illustration of a rectangular domain with the boundary subdivided into eight elements. Spatial collocation points indicated by dots are located at the centre of each element. Arrows indicate collocation points in the direction variable p.

2.3. Extension to multi-domain problems

A generalisation to multi-domain problems, with convex sub-domains Ω_α, $\alpha = 1, \ldots, N_\Omega$, follows by introducing a multi-domain boundary integral operator

$$\mathcal{L}_\sigma^{\alpha,\beta} g(X^\alpha) = \int_{Q_\beta} w^{\alpha,\beta}(X^\alpha, Y^\beta) f_\sigma(X^\alpha - \varphi^{\alpha,\beta}(Y^\beta)) g(Y^\beta) \, dY^\beta. \tag{9}$$

The operator $\mathcal{L}_\sigma^{\alpha,\beta}$ transports a phase-space density g from the boundary phase-space of Ω_β (denoted Q_β) to the boundary phase-space of Ω_α via the multi-domain boundary map $\varphi^{\alpha,\beta}$. We have also introduced the notation $X^\alpha = (s^\alpha, p^\alpha)$ and $Y^\alpha = (t^\alpha, q^\alpha)$ for the phase-space coordinates on the boundary of Ω_α. The domain $\Omega = \cup_{\alpha=1}^{N_\Omega} \Omega_\alpha$ becomes the union of all sub-domains and Γ becomes the union of all sub-domain boundaries, thus $\Gamma = \cup_{\alpha=1}^{N_\Omega} \partial \Omega_\alpha$. The global stochastic propagation operator $\mathcal{L}_\sigma$ is then constructed from the set of inter-domain operators $\mathcal{L}_\sigma^{\alpha,\beta}$. Note that the case of transporting the density within a sub-domain is included in this formulation when $\alpha = \beta$. Otherwise, the direct transfer of the energy via the density ρ will only take between neighbouring sub-domains with a common boundary region or interface through which the density can be transported.

If the properties of two neighbouring sub-domains Ω_α and Ω_β are different, for example if $c_\alpha \neq c_\beta$, where c_α is the propagation speed in Ω_α (likewise for c_β in Ω_β), then reflection/transmission probabilities $\lambda_{\alpha,\beta}$ (or even mode conversion probabilities for vectorial elasticity problems) must be included in the weight function $w^{\alpha,\beta}$ to account for the probability of transmission or reflection at the common interface. The reflection/transmission probability term $\lambda_{\alpha,\beta}$ thus satisfies $\lambda_{\alpha,\beta} = 1 - \lambda_{\beta,\beta}$ at the interface between the sub-domains Ω_α and Ω_β, see Fig. 1. For propagating scalar waves, the reflection/transmission probabilities correspond to the well-known Fresnel equations from optics together with Snell's Law of refraction, see for example [34,35]. For given Y^β on the boundary of Ω_β, we may again interpret the evolution given by the operator $\mathcal{L}_\sigma^{\alpha,\beta}$ as originating from a stochastic (multi-domain) boundary map $\varphi_\sigma^{\alpha,\beta}$ defined by

$$\varphi_\sigma^{\alpha,\beta}(Y^\beta) = X^\alpha$$
$$= \varphi^{\alpha,\beta}(Y^\beta) + X_\varepsilon^\alpha,$$

where $X_\varepsilon^\alpha = (s_\varepsilon^\alpha, p_\varepsilon^\alpha)$ are random variables drawn from the PDF f_σ for the sub-domain Ω_α. For simplicity, we will restrict to the case that all sub-domains have the same PDF.

3. Discretisation

In this section we detail the discretisation of the boundary integral equation (3) using the collocation method. For illustration purposes we consider a single polygonal domain, such as the rectangle depicted in Fig. 2. Here, the spatial collocation points have been indicated by dots at the centre of each element and the arrows show the collocation directions taken for the momentum variable p. The phase-space ray flow map φ will be discontinuous at corners of Ω and hence a piecewise constant basis approximation is employed in the spatial variable s. The approximation of the energy density $\rho(X)$ on the boundary Γ may therefore be written in the form

$$\rho(X) \approx \sum_{j=1}^{n} b_j(s) \rho_j(p), \tag{10}$$

where n is the total number of boundary elements, $b_j(s) = 1$ if s lies on the jth element and is zero elsewhere, and $\rho_j(p)$ are a set of p-dependent functions. Substituting the approximation (10) for ρ into (1) in place of the density g and then applying a quadrature method with respect to the variable p would lead to a Nyström method in the momentum variable as studied in Refs. [36,30]. The size of the matrix representation of the operator $\mathcal{L}_\sigma$ will be proportional to the number of quadrature nodes in this case. In this work we instead apply the collocation method to discretise with respect to the variable p, which has the advantage that we can separate the dependence of the matrix size (which now instead depends on the number of collocation points) from the number of quadrature nodes used to approximate the integral. This may be

particularly favourable in the small σ regime close to the deterministic dynamics, where the integral kernel f_σ in Eq. (7) undergoes a singular perturbation and will hence require a large number of quadrature nodes in general.

3.1. Phase-space collocation method

The collocation method is now applied in the variable p by making a finite dimensional basis approximation of the directionally dependent functions $\rho_j(p)$ appearing in (10). That is

$$\rho_j(p) \approx \sum_{l=1}^{N+1} \rho_{j,l} \phi_l(p), \tag{11}$$

where $\rho_{j,l}$ are the unknown basis expansion coefficients to be determined and $\phi_l(p)$, $l = 1, \ldots, N+1$ denotes the set of p-dependent basis functions. Substituting the full basis approximation (10)–(11) for ρ into (1) in place of the density g we obtain

$$\mathcal{L}_\sigma \rho(X) \approx \sum_{j=1}^{n} \sum_{l=1}^{N+1} \rho_{j,l} \left[\int_Q f_\sigma(X - \varphi(Y)) b_j(t) \phi_l(q) \, dY \right]$$

$$= \sum_{j=1}^{n} \sum_{l=1}^{N+1} \rho_{j,l} \left[\int_{-c^{-1}}^{c^{-1}} \phi_l(q) \left[\int_{I_j} f_\sigma(X - \varphi(Y)) \, dt \right] dq \right],$$

where I_j denotes the jth boundary element. Substituting in the formula (7) for the PDF f_σ leads to

$$\mathcal{L}_\sigma \rho(X) \approx \sum_{j=1}^{n} \sum_{l=1}^{N+1} \rho_{j,l} \left[\int_{-c^{-1}}^{c^{-1}} \phi_l(q) f_{\sigma_2}(p_\varepsilon) \left[\int_{I_j} f_{\sigma_1}(s_\varepsilon) \, dt \right] dq \right],$$

$$= \sum_{j=1}^{n} \sum_{l=1}^{N+1} \rho_{j,l} \left[\int_{-c^{-1}}^{c^{-1}} \phi_l(q) f_{\sigma_2}(p_\varepsilon) \left[-\frac{1}{2\psi_{\sigma_1}} \mathrm{erf}\left(\frac{s - \varphi_s(t)}{\sqrt{2}\sigma_1} \right) \Big|_{t_{\min}(q)}^{t_{\max}(q)} \right] dq \right], \tag{12}$$

where the spatial integral has now been expressed analytically as a function of q. The limits $t_{\min}$ and $t_{\max}$ lie at the end points of (or inside) the jth boundary element I_j; if the limit is inside the element then it corresponds to the pre-image of a vertex of the domain for rays with direction q. Note that the spatial integral can also be treated analytically (by parts) in terms of the error function erf if we include an additional spatially dependent damping factor of the form $\exp(-\mu d(\varphi_s(t), t))$, with notation as in Sect. 2. This is a consequence of the fact that the Euclidean distance $d(\varphi_s(t), t)$ between two points on the boundary of a polygon may be expressed as a linear function of t when q is fixed. In what follows, we denote the spatial integral over the jth boundary element as S_μ^j. Unfortunately, the analytical expression for S_μ^j when $\mu > 0$ is not always numerically robust for all geometries and values of σ_1. In such cases the spatial integral can be well approximated by high order quadrature methods. Note also that the analytical expression for S_μ^j remains bounded for $\sigma_1 = 0$, even though the PDF f_σ is unbounded in this case.

Recall that the spatial basis approximation uses piecewise constant functions defined according to a decomposition of Γ into boundary elements and therefore only one collocation point per element is required. We choose these points to be located at the centre of the corresponding boundary element as shown in Fig. 2, and denote them s_i, $i = 1, \ldots, n$. The collocation points in the direction variable are taken to be the Chebyshev points

$$p_k = c^{-1} \cos\left(\frac{2k-1}{2(N+1)} \pi \right), \quad k = 1, \ldots, N+1,$$

which leads to equi-distributed direction angle collocation points

$$\theta_k = \frac{\pi}{2} - \frac{2k-1}{2(N+1)} \pi.$$

The choice of Chebyshev collocation points minimises the effect of Runge's phenomenon, see for example [37], Ch. 5. The full collocation discretisation of equation (1) for the density $g = \rho$ is therefore given by $(\mathcal{L}_\sigma \rho)(s_i, p_k) \approx L\boldsymbol{\rho}$, where the vector $\boldsymbol{\rho} = [\rho_{1,1} \ \rho_{1,2} \cdots \rho_{1,N+1} \ \rho_{2,1} \cdots \rho_{n,N+1}]^T$ is formed from the coefficients $\rho_{j,l}$ and the entries of the matrix L are given by

$$L_{(i,k),(j,l)} = c^{-1} \int\limits_{-\pi/2}^{\pi/2} \phi_l(q(\theta')) f_{\sigma_2}(p_\varepsilon(p_k, \theta')) S_\mu^j(s_i, q(\theta')) \cos(\theta') \, d\theta', \tag{13}$$

with $p_\varepsilon(p_k, \theta') = p_k - c^{-1} \sin(\theta')$ for $i, j = 1, ..., n$ and $k, l = 1, ..., N + 1$. Note that we have changed the integration variable from $q(\theta') = c^{-1} \sin(\theta')$ to the direction angle θ'. In the multi-domain case we would additionally include reflection/transmission probabilities $\lambda_{\alpha,\beta}$ inside the integral in (13) when the collocation point s_i is on the common interface between two neighbouring sub-domains.

We apply adaptive Clenshaw–Curtis quadrature for computing the integrals over θ' in (13). We find that Clenshaw–Curtis quadrature exhibits spectral convergence, even in the case of small $\boldsymbol{\sigma}$ values, provided that a careful subdivision procedure is implemented to ensure the smoothness of each sub-integrand. The polygonal nature of the computational domain and the piecewise constant approximation in space mean that the direction dependent function S_μ^j will become discontinuous at a finite number of discrete points, but is piecewise smooth away from these points. Therefore we subdivide the integral over θ' for the jth boundary element into subintervals with respect to the directions from the endpoints of the element j to all vertices of the polygon Ω and all spatial collocation points.

The discretised form of equation (3) can now be written as a linear system

$$(K - L)\boldsymbol{\rho} = K\boldsymbol{\rho}_0. \tag{14}$$

Here K is an $n(N+1) \times n(N+1)$ interpolation matrix, which maps the basis coefficients $\boldsymbol{\rho}$ to the values of the density ρ at the collocation points. Hence the right hand side of (14) corresponds to the source density evaluated at the collocation points in both position and direction, where $\boldsymbol{\rho}_0$ is the vector of basis coefficients for the projection of the source density onto the finite dimensional space spanned by the spatial and momentum basis functions. Explicitly, K takes the form of a sparse block matrix

$$K = \begin{bmatrix} \Phi & 0 & \cdots & 0 \\ 0 & \Phi & \cdots & 0 \\ \vdots & \vdots & \ddots & \vdots \\ 0 & 0 & \cdots & \Phi \end{bmatrix}$$

consisting of n identical $(N+1) \times (N+1)$ blocks Φ along the diagonal (and zeros otherwise) where

$$\Phi_{k,l} = \{\phi_l(p_k)\} \text{ for } k, l = 1, ..., N + 1. \tag{15}$$

In the next section we discuss different options for the choice of basis functions ϕ_l.

3.2. Basis approximation in the direction variable

Orthogonal polynomials, such as Legendre or Chebyshev polynomials, are popular choices for approximating smooth functions on finite intervals due to their spectral convergence [38]. In what follows we restrict our discussion to Legendre polynomials; initial tests conducted with Chebyshev polynomials did not lead to any qualitative differences in the numerical results.

In general it will be more computationally expensive to obtain accurate results in the small $\boldsymbol{\sigma}$ regime close to the deterministic dynamics, where the integral kernel f_σ in Eq. (7) undergoes a singular perturbation. As an alternative approach, we will therefore consider Gaussian radial basis functions of the form

$$\boldsymbol{\phi}_l(p_k) = \exp\left(-\frac{(p_k - p_l)^2}{2\sigma_2^2}\right), \quad l = 1, ..., N + 1, \tag{16}$$

for given p_k, where $k = 1, ..., N + 1$ and σ_2 is as before. The potential appeal of this choice of basis stems from the fact that directionally uncertain (Gaussian distributed) boundary conditions can be represented exactly in this basis, see Sect. 4, and therefore it may be possible to achieve reasonable accuracy for small σ_2 values relatively efficiently. In addition, the interpolation of smooth functions with Gaussian radial basis functions may also exhibit spectral convergence [39]. Furthermore, the interpolation matrix K for the Gaussian radial basis functions is symmetric and positive definite providing a unique solution. However, the local interpolation matrix Φ (15) is numerically ill-conditioned and hence preconditioning is required, particularly for high orders of approximation and/or large values of σ_2 ([39], Ch. 2). We address this issue in the following section.

3.3. Preconditioning for Gaussian radial basis functions

In this section we discuss how we construct a preconditioning matrix for the Gaussian radial basis functions introduced in the last section. We define a preconditioning matrix P in the same block form as the interpolation matrix K. In this case we label the n non-zero blocks of size $(N+1) \times (N+1)$ located along the diagonal as M, that is

---

Algorithm 1 Construct the preconditioning matrix M.

1: Perform the eigen-decomposition $\Phi = X\Lambda X^{-1}$ and initialise $M^{(0)} = I$.
2: Find $\lambda_{\max} = \max\{\Lambda\}$ and $\lambda_{\min} = \min\{\Lambda\}$.
3: Solve

$$\frac{1 - (1 - \lambda_{\max})^{2^\kappa}}{1 - (1 - \lambda_{\min})^{2^\kappa}} = \sqrt{\frac{\lambda_{\max}}{\lambda_{\min}}}$$

   to find the optimal positive integer value for κ.
4: **for** $l = 1, ..., \kappa$ **do**
5:    Compute $M^{(l)} = M^{(l-1)}(2I - \Lambda M^{(l-1)})$.
6: **end for**
7: Update the preconditioner $M^{(\kappa)} \leftarrow X M^{(\kappa)} X^{-1}$.
8: **return** M

$$P = \begin{bmatrix} M & 0 & \cdots & 0 \\ 0 & M & \cdots & 0 \\ \vdots & \vdots & \ddots & \vdots \\ 0 & 0 & \cdots & M \end{bmatrix}.$$

The preconditioned linear system is written as

$$(K - L)P\tilde{\boldsymbol{\rho}} = KP\tilde{\boldsymbol{\rho}}_0,$$

where the solution of the original system (14) can be recovered via $\boldsymbol{\rho} = P\tilde{\boldsymbol{\rho}}$ and likewise, $\boldsymbol{\rho}_0 = P\tilde{\boldsymbol{\rho}}_0$. We note that due to the sparse repeated block structure of both K and P, the preconditioning can be performed most efficiently by working locally and block-wise. To do this we instead solve the equivalent system

$$(I - \tilde{L})\tilde{\boldsymbol{\rho}} = \tilde{\boldsymbol{\rho}}_0,$$

with the modified transfer operator matrix $\tilde{L} = (KP)^{-1}LP$. The block structure of K and P means that the matrix $\tilde{L}$ may be assembled from n^2 sub-blocks of size $(N+1) \times (N+1)$ by pre-multiplying the corresponding sub-block of L by $(\Phi M)^{-1}$ and post-multiplying by M, meaning that the global matrices K and P are never formed.

We now follow the approach presented in Ref. [40] and choose M as a truncated Neumann series with an integer parameter κ thus:

$$M := M^{(\kappa)} = \sum_{m=0}^{2^\kappa - 1} (I - \Phi)^m. \tag{17}$$

Notice that if $\kappa = 0$ then $M = I$ and in the limit when $\kappa \to \infty$ we obtain $M = \Phi^{-1}$, where Φ is given by (15). Neither of these limit cases are suitable for the choice of preconditioning. Thus we need to find an optimal value for κ such that condition number of the matrix ΦM approximately coincides with the condition number of the matrix M. This is because the matrix P also enters the computation of the matrix system via $\tilde{L} = (KP)^{-1}LP$ and therefore may affect the accuracy. The ideal number of iterations κ can be estimated by solving the non-linear equation

$$\frac{1 - (1 - \lambda_{\max})^{2^\kappa}}{1 - (1 - \lambda_{\min})^{2^\kappa}} = \sqrt{\frac{\lambda_{\max}}{\lambda_{\min}}},$$

where $\lambda_{\min}, \lambda_{\max} > 0$ are the minimal and maximal eigenvalues of the matrix Φ, respectively. The procedure is listed in Algorithm 1, where one eigenvalue decomposition of the matrix Φ is required to find the optimal κ, while at the same time replacing matrix multiplication operations by vector products to obtain the preconditioning matrix M. The appearance of $2^\kappa - 1$ (rather than simply κ) as the upper limit of the summation in (17) is a consequence of the fact that we employ the accelerated iterative strategy presented in Ref. [40] to form M, see steps 4 to 6 of Algorithm 1. If the same directional collocation points are used on each element and the values of c and σ_2 are kept constant, then the computation of the matrix M is required only once during the preprocessing. Importantly, Algorithm 1 converges only if $\|\Phi\| < 1$ and, in general, scaling must therefore be applied before the algorithm can be implemented. For more details see Ref. [40].

4. Implementation and convergence of the collocation method

In this section we study the implementation of the collocation method described above, initially via a simple intuitive example, before we proceed with a more detailed convergence study. We perform numerical tests for a rectangular domain consisting of the points $\mathbf{r} = (r_1, r_2) \in (0, a) \times (0, 0.25)$ with an uncertain boundary source
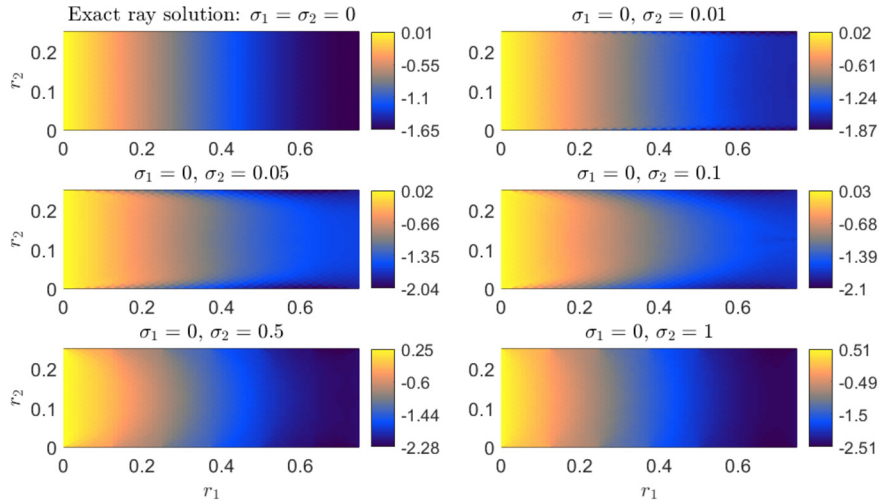
Fig. 3. Logarithm of the energy density inside a rectangular domain obtained from a deterministic (top left) and uncertain (others) boundary source prescribed at the left edge of the rectangle. Top left: exact ray solution when $\sigma_1 = \sigma_2 = 0$. Others: numerical results when $\sigma_1 = 0$, $\sigma_2 > 0$, $n = 16$ and $N = 256$. Parameter values: $\omega = 200\pi$, $c = 1$ and $\eta = 0.01$.

$$\rho_0(s, p) = \frac{\exp\left(-p^2/(2\sigma_2^2)\right) \chi_{\{r_1(s)=0\}}(s)}{\sqrt{2\pi\sigma_2^2} \, \mathrm{erf}\left(1/(\sqrt{2}\sigma_2 c)\right)}, \tag{18}$$

where $\chi_{\{r_1(s)=0\}}$ is used to denote the restriction of the source density to the left hand edge at $r_1 = 0$. In particular, since s is used to denote the position coordinate on the boundary parametrised by arc-length, then here $s \in [0, 2a + 0.5)$ and if we take $s = 0$ at the origin then $\chi_{\{r_1(s)=0\}} = 0$ unless $s \in [2a + 0.25, 2a + 0.5) \cup \{0\}$, where $\chi_{\{r_1(s)=0\}} = 1$. For small σ_2, then (18) corresponds to a unit boundary density propagating (on average) in the direction $p = 0$, that is, in the direction of the interior unit normal vector at s. For large σ_2 it corresponds to randomly directed propagation from the boundary. A homogeneous Neumann boundary condition will be assumed over the rest of the boundary Γ. This problem possesses an analytical ray tracing solution for the interior density ρ_Ω when $\boldsymbol{\sigma} \to \mathbf{0}$, which is given by

$$\rho_\Omega(\mathbf{r}) = \frac{e^{-\mu r_1} + e^{-\mu(2a - r_1)}}{1 - e^{-2\mu a}}. \tag{19}$$

Here $\mu = \eta\omega/(2c)$ is a frequency-dependent dissipation rate with (hysteretic) loss factor η and angular frequency ω. In what follows we choose $c = 1$, $a = 0.75$, $\eta = 0.01$ and $\omega = 200\pi$ unless otherwise specified.

The upper-left plot of Fig. 3 shows the exact ray solution (19), whilst in the other plots we illustrate our numerical approximations of the (logarithm of the) interior energy density (5) for different values of σ_2 and with $\sigma_1 = 0$. In the numerical simulations here we used $n = 16$ spatial collocation points and a Legendre polynomial basis with 257 collocation points ($N = 256$) for the discretisation with respect to the momentum variable. A high degree polynomial approximation in momentum is required to accurately model the propagation described by the Gaussian f_{σ_2}, since f_{σ_2} develops an increasingly sharp peak when σ_2 becomes very small. We will see in Sect. 4.2 that this situation can be improved to some extent by employing a Gaussian radial basis approximation instead.

The effect of taking $\sigma_2 > 0$ is that the rays then begin to reflect from the upper and lower edges of the rectangle, increasing the average total length of a trajectory traversing between the left and right edges and meaning that trajectories leaving the left edge boundary source will stay relatively close to the left edge for longer. Since dissipation has been applied in the form of an exponential decay factor along the trajectory length, then it is clear why larger values of σ_2 lead to faster decay of the ray density from left to right and a greater ray density close to the boundary line source on the left; this is illustrated by the colour scales in Fig. 3. Note that larger values of σ_2 not only increase the spreading of rays from the boundary source, but also increase the uncertainty in the direction of each subsequent reflection at the boundary. Fig. 3 therefore demonstrates the transition in the solution behaviour from the deterministic directivity of the upper-left plot, to a random reflection model in the lower-right plot.

4.1. Convergence rates for the approximation of the boundary density

In this section we study the convergence properties of the bivariate collocation method detailed above. Equation (3) is a Fredholm integral equation of the second kind on the boundary phase-space Q. Hence we can make use of the theory presented in Ref. [31] to estimate the convergence rate for our bivariate collocation scheme on polygonal domains Ω. In
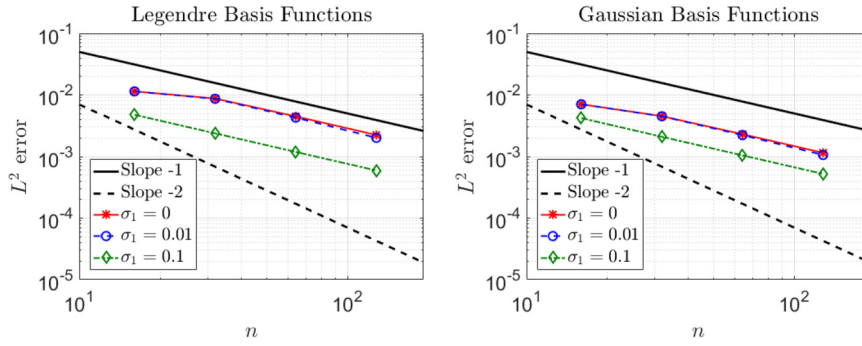
Fig. 4. The L^2 error of the stationary boundary density ρ versus the number of spatial collocation points n estimated using the difference between the solutions computed with n and $2n$ boundary elements. The results have been computed on a rectangular domain with three different σ_1 values and a fixed number of collocation points in the momentum discretisation. Parameter values: $N = 64$, $\sigma_2 = 0.1$, $\omega = 200\pi$, $c = 1$ and $\eta = 0.01$. Left: orthogonal Legendre polynomial basis approximation in momentum. Right: Gaussian radial basis approximation in momentum.

particular, since the PDF f_σ (7) is bounded on Q for fixed $\sigma_1, \sigma_2 > 0$, then the operator $\mathcal{L}_\sigma : L^2(Q) \to L^2(Q)$ is bounded. Let us denote the multivariate collocation projection operator as $\mathcal{P}_n$, where $\boldsymbol{n} = (n, N)$. Under the assumptions that $I - \mathcal{L}_\sigma$ is invertible and $\|\mathcal{L}_\sigma - \mathcal{P}_n \mathcal{L}_\sigma\| \to 0$ as $n, N \to \infty$, then based on Theorem 3.1.1 of Ref. [31] we can expect the solution to the discretised problem (14) to converge at the same rate as the projection

$$(\mathcal{P}_n \rho)(s, p) = \sum_{j=1}^{n} \sum_{l=1}^{N+1} \rho_{j,l} b_j(s) \phi_l(p) \tag{20}$$

converges to the true solution $\rho \in L^2(Q)$. The norm notation here refers to the $L^2(Q) \to L^2(Q)$ operator norm. Hence for our combined space and momentum discretisation scheme we could expect first order convergence with respect to the mid-point collocated piecewise constant approximation in space [31] and potentially even spectral convergence for the approximations in momentum described in Sect. 3.2. We note that the invertibility assumption will follow via a Neumann series argument provided that $\|\mathcal{L}_\sigma\| < 1$, which is true given a large enough dissipation/damping factor $\mu > 0$. More details on the necessary assumptions are provided in Appendix A. We note also that the theory in Sect. 3.6.1 of Ref. [31] may be applied to study the conditioning of the matrix equation (14). In particular, an upper bound on the condition number for the collocation method is established, which includes a factor of the matrix norm of the inverse interpolation matrix K^{-1}. It is this term that can grow large for the Gaussian radial basis and thus necessitates a preconditioning strategy, such as the one detailed in Sect. 3.3. In the remainder of this section we investigate the convergence rates for the proposed phase-space collocation method in practice, through a series of numerical experiments.

We first study the convergence of the spatial discretisation in isolation with a fixed truncation at $N = 64$ for the momentum basis using both Legendre polynomials and Gaussian radial basis functions. We consider the rectangular domain from before with the uncertain boundary source (18) for $\sigma_2 = 0.1$ and three different values of σ_1, including $\sigma_1 = 0$ when the convergence theory from Ref. [31] no longer applies. Fig. 4 shows the L^2 norm of the difference between the stationary boundary density solutions ρ computed with n and $2n$ boundary elements, for a range of values of n.

The error plots in Fig. 4 indicate that the collocation method in space is converging approximately linearly as expected for the piecewise constant basis approximation. We observe a similar rate of convergence for both choices of momentum basis, but with lower error values for the Gaussian basis. Note that there is also only a very minor slow down in the convergence rate for the case when $\sigma_1 = 0$ and the error values themselves are almost indistinguishable from the case when $\sigma_1 = 0.01$. This suggests that the predicted linear convergence rates also hold even for $\sigma_1 = 0$ when f_σ becomes unbounded. The lowest errors are found in the case when $\sigma_1 = 0.1$. This is most likely due to the higher level of uncertainty in the spatial propagation leading to a more even spreading of the rays across the domain, and hence the ray density exhibits a slower spatial variation that can be better represented by the piecewise constant basis approximation.

We now consider the convergence of the direction approximation by repeating the previous set of numerical experiments for a fixed number of spatial collocation points $n = 16$. Fig. 5 shows the L^2 norm of the difference between the stationary boundary density solutions ρ computed with $N + 1$ and $2N + 1$ collocation points in direction, for a range of values of N. We perform the study for both the Legendre polynomial basis and the Gaussian radial basis, as before.

The error plots in Fig. 5 indicate that the collocation method in direction is converging spectrally as we conjectured for the two choices of basis expansion considered. For the Gaussian radial basis approximation, the errors for smaller numbers of collocation points are lower compared to the corresponding errors using Legendre basis functions. This can be attributed to the fact that boundary source (18) for this example is exactly represented by the Gaussian radial basis functions (16) when $p_l = 0$. On the other hand, the numerical simulations using Gaussian radial basis functions do not converge to machine precision due to the presence of conditioning errors, despite the preconditioning process. The error values do however reach single precision, which is sufficient for most engineering applications. A further interesting feature
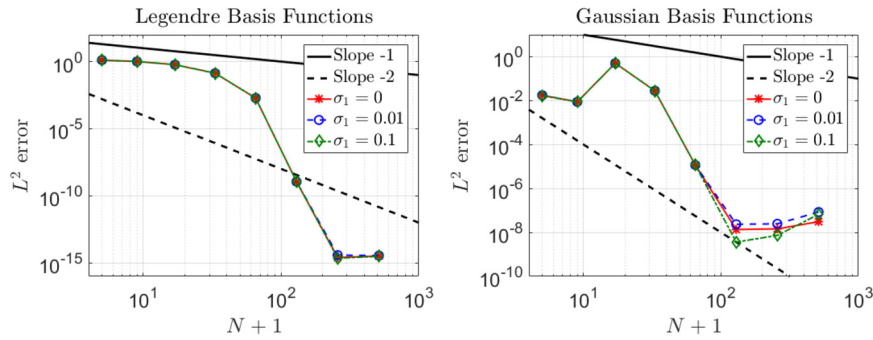
Fig. 5. The L^2 error of the stationary boundary density ρ versus the number of collocation points for the momentum discretisation estimated using the difference between the solutions computed with $N + 1$ and $2N + 1$ collocation points. Results have been computed on a rectangular domain with three different σ_1 values and a fixed number of spatial collocation points. Parameter values: $n = 16$, $\sigma_2 = 0.1$, $\omega = 200\pi$, $c = 1$ and $\eta = 0.01$. Left: orthogonal Legendre polynomial basis approximation in momentum. Right: Gaussian radial basis approximation in momentum.

of the results for the Gaussian basis is the increase in the error between $N = 8$ and $N = 16$. This can also be identified as a conditioning error since for small N, the conditioning of the system is relatively good and the optimal value of the parameter κ is zero for $N = 4, 8$, meaning that no preconditioning is necessary. For $N > 8$, the conditioning becomes worse and leads to an increase in the error that is reduced, but not fully eradicated, by the preconditioning. Note that once again, the convergence rates appear to be independent of the σ_1 values. In the next section we consider the behaviour of the collocation discretisation as $\boldsymbol{\sigma} \to \mathbf{0}$ with reference to the exact solution when $\boldsymbol{\sigma} = \mathbf{0}$.

4.2. Convergence to the interior density when $\boldsymbol{\sigma} \to \mathbf{0}$

In the previous section we demonstrated the convergence properties of the collocation method for the boundary density ρ. In this section we study convergence to the exact ray tracing solution (19) for the interior density ρ_Ω when $\boldsymbol{\sigma} \to \mathbf{0}$, and compare the Legendre and Gaussian basis approximations. The convergence properties for ρ_Ω, which is computed from the boundary density ρ via equation (5), are considered at three arbitrarily chosen interior points: $A = (0.1, 0.2)$, $B = (0.4, 0.1)$ and $C = (0.6, 0.15)$. Note that due to its one-dimensional nature, the exact solution is constant along the left and right edges of the rectangle and zero along the upper and lower boundary edges. Hence we employ a relatively coarse boundary element mesh with only $n = 8$ piecewise constant boundary elements. In addition, we set $\sigma_1 = 0$ and consider only the limit $\sigma_2 \to 0$.

Fig. 6 shows the discrepancy between the numerical solution for the interior density with different values of $\sigma_2 > 0$ and the exact solution for $\boldsymbol{\sigma} = \mathbf{0}$. We note that this discrepancy is computed as a relative error for different numbers of collocation points N for the momentum discretisation relative to the exact solution by taking the absolute value of the discrepancy and dividing by the absolute value of the exact solution. In the left column we show the results for the Legendre basis approximation, while in the right column we show the results for the Gaussian radial basis approximation. The discrepancy plots for fixed values of σ_2 will eventually flatten as the number of collocation points is increased, and the difference between the numerical and analytical solutions then remains approximately constant for all larger values of N. The value of this constant reflects the true discrepancy between the exact solution for $\sigma_2 = 0$ and the numerical solution for $\sigma_2 > 0$. Note that for the smaller choices of σ_2, the relative errors (or discrepancies) are still several orders of magnitude smaller than those typically attained using the corresponding deterministic transfer operator model with $\sigma_2 = 0$; see Ref. [41] for a three-dimensional realisation of this same (effectively one-dimensional) example. It should be noted that in this case the corresponding boundary transfer operator is non-compact and the corresponding convergence theory is far less developed.

From Fig. 6 we notice that the discrepancies for large values of N appear to be almost identical for both choices of the basis functions. We would expect this to be the case since both basis approximations should converge to the same numerical solution for each $\sigma_2 > 0$. We also observe that the numerical solutions are converging to the exact ray tracing solution (19) when $\boldsymbol{\sigma} \to \mathbf{0}$ since the values of the large N discrepancies are decreasing as $\sigma_2 \to 0$. We notice that the gradual convergence for small N values often becomes a sharp drop as N is increased, again suggesting a super-algebraic convergence rate. However, it is also clear that for smaller values of σ_2 we must employ more collocation points to observe this convergence. For small N we find that the discrepancies are much lower for the Gaussian radial basis approximation, even by as much as five orders of magnitude when $N = 4$. The small N errors for the Gaussian basis are particularly impressive for the smaller σ_2 values where the Legendre basis performs relatively badly. The performance of the Gaussian basis can be attributed to the fact that the Gaussian radial basis functions represent the uncertain boundary source term (18) exactly when $p_l = 0$ in equation (16), including the sharp peak when σ_2 is small. This leads to solutions with acceptable engineering level accuracy using relatively few basis functions since one obtains convergence to the numerical solution for $\sigma_2 > 0$ with small N (this can be observed by comparison to the minimal discrepancy provided by the Legendre basis for a particular $\sigma_2 > 0$ and
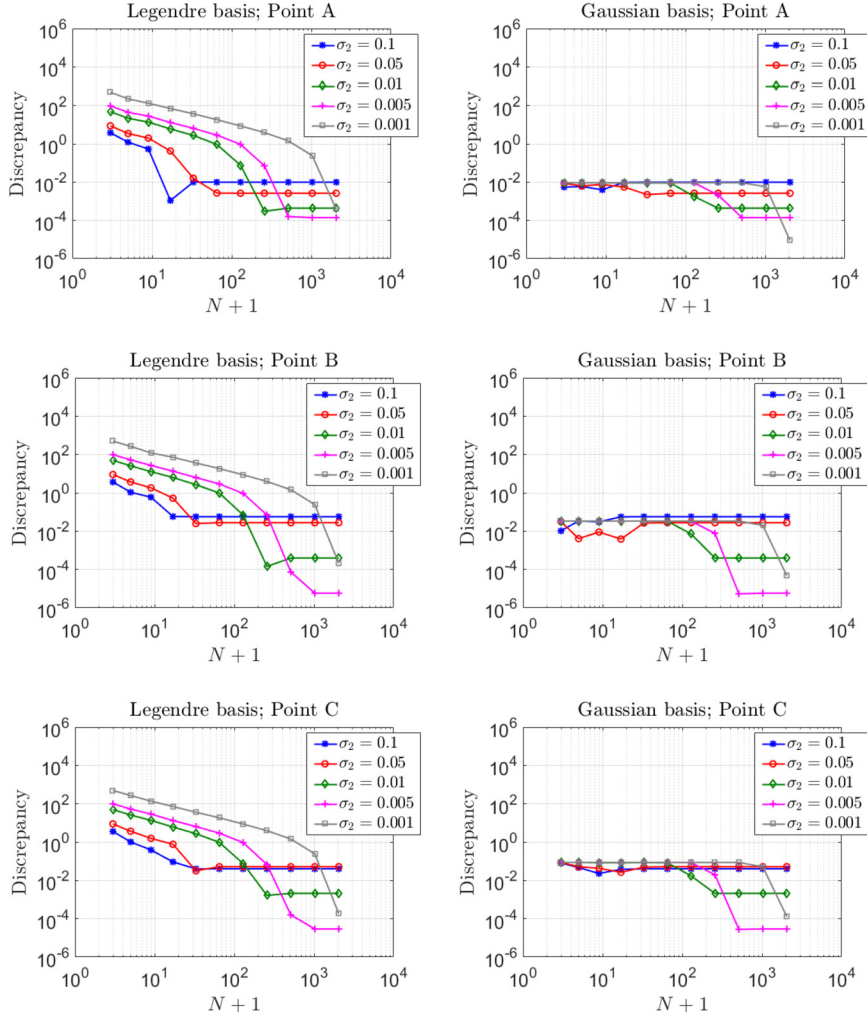
Fig. 6. Convergence of the interior density to the exact ray tracing solution with $\sigma = 0$ at three points $A = (0.1, 0.2)$, $B = (0.4, 0.1)$ and $C = (0.6, 0.15)$. Note that for the discrepancy between the numerical solution and the exact solution to decay we need to both decrease σ_2 and increase N. Left: Legendre basis approximation in momentum. Right: Gaussian radial basis approximation in momentum. Parameter values: $n = 8$, $\sigma_1 = 0$, $\omega = 200\pi$, $c = 1$ and $\eta = 0.01$.

large N). On the other hand, as σ_2 is decreased and the peak at $p_k = 0$ increases in height and narrows in width, the low order polynomial interpolation provided by the Legendre basis for small N will perform progressively worse.

In summary, both choices of basis approximation in the direction variable can lead to spectral convergence and a Gaussian radial basis will be beneficial for source dominated problems with relatively simple directional dependence. In particular, the success of the Gaussian radial basis here is a direct consequence of the fact that it can exactly represent the source density (18) at very low truncation order. Whilst this could be viewed as a limitation of the proposed approach to source densities of the form (18), the principle on which the approach is based may be generalised: a basis that can exactly represent the source density at low order can potentially lead to a more efficient discretisation method. Furthermore, such an approach may be particularly appealing when the source is not efficiently represented by a conventional orthogonal polynomial basis, which is the case for the Gaussian source here when σ_2 is very small. However, due to the simpler implementation procedure, in the sequel we employ the Legendre polynomial basis for problems with point sources in more complex and irregular multi-domains where there will be no clear advantage in employing the Gaussian basis.

5. Numerical results for multi-domain problems

In this section we compute the acoustic energy density distribution given by our stochastic propagation model in a series of three coupled two-dimensional domains taken from Refs. [9,42]. An acoustic velocity potential point source is used as the excitation term for these problems, which gives rise to a corresponding phase-space energy density source on the boundary ρ_0 given by [10]

Table 1

Vertex and source point coordinates of the three coupled domain configurations. The interface between the sub-domains Ω_1 (on the left) and Ω_2 (on the right) is taken to be the line $r_1 = 0$.

Vertex	Configuration A		Configuration B		Configuration C	
	r_1	r_2	r_1	r_2	r_1	r_2
1	1.4564	0.40381	1.4564	0.40381	1.4564	0.40381
2	0.87	1.1027	0.87	1.1027	0.87	1.1027
3	0.0	0.6993	0.0	0.7993	0.0	0.9493
4	−0.83	1.1720	−1.503	0.7993	−0.83	1.1720
5	−1.048	0.3582	−1.503	0.1993	−1.048	0.3582
6	−0.28	0.0	0.0	0.1993	−0.28	0.0
7	0.0	0.2993	0.69	−0.1328	0.0	0.0493
8	0.69	−0.1328			0.69	−0.1328
Source	−0.4	0.5	−1.4	0.4993	−0.4	0.5

$$\rho_0(s, p; \mathbf{r}_0) = \frac{\omega \rho^f \cos(\vartheta(s, \mathbf{r}_0)) e^{-\mu|\mathbf{r}_s - \mathbf{r}_0|}}{8\pi |\mathbf{r}_s - \mathbf{r}_0|} \delta(p - p_0), \tag{21}$$

where $\mathbf{r}_0$ is the position vector of the source point, ρ^f is the density of the acoustic medium and $\vartheta(s, \mathbf{r}_0)$ is minus the angle that the vector from $\mathbf{r}_0 \in \Omega$ to $s \in \Gamma$ makes with the interior unit normal vector at s. In addition, $\mathbf{r}_s$ is the position vector of the point $s \in \Gamma$, $p_0 = \sin(\vartheta(s, \mathbf{r}_0))/c$ is the tangential component of the slowness vector (at $s \in \Gamma$) for the ray trajectory arriving from the source point $\mathbf{r}_0$ and $\mu = \eta \omega/(2c)$ is the (viscous) damping factor as before.

The formula (21) assumes that the source has been transported deterministically from the source point to the boundary. If we instead transport the source to the boundary via propagation according to the probability density function (7) then we obtain

$$\rho_0(s, p; \mathbf{r}_0) = \frac{\omega \rho^f}{8\pi} \int_\Gamma \frac{e^{-\mu|\mathbf{r}_t - \mathbf{r}_0|}}{|\mathbf{r}_t - \mathbf{r}_0|} \cos(\vartheta(t, \mathbf{r}_0)) f_{\boldsymbol{\sigma}}(s_\varepsilon(t), p_\varepsilon(t)) \, dt, \tag{22}$$

where $s_\varepsilon = s - t$, $p_\varepsilon = p - p_0(t)$ and $p_0(t) = \sin(\vartheta(t, \mathbf{r}_0))/c$. Note that in the special case when $\sigma_1 \to 0$, then the formula (22) reduces to

$$\rho_0(s, p; \mathbf{r}_0) = \frac{\omega \rho^f \cos(\vartheta(s, \mathbf{r}_0)) e^{-\mu|\mathbf{r}_s - \mathbf{r}_0|}}{8\pi |\mathbf{r}_s - \mathbf{r}_0|} \frac{\exp\left(-\dfrac{(p - p_0)^2}{2\sigma_2^2}\right)}{\sqrt{2\pi} \sigma_2 \psi_{\sigma_2}(p^-, p^+)},$$

and it is clear that the original expression (21) is returned in the limit $\sigma_2 \to 0$.

We apply the point source expression (22) as our initial boundary density in the subsequent numerical studies. The vertices and source point coordinates for the three configurations considered are listed in Table 1. All three configurations, together with their corresponding numerical results, can be seen in Figs. 7 to 9. In each case we investigate the energy ratio between the left sub-domain Ω_1 and the right sub-domain Ω_2, and in particular its dependence on the frequency $f = \omega/(2\pi)$Hz, as well as the values taken for the uncertainty parameters $\boldsymbol{\sigma}$. The total energy in each sub-domain is given by

$$P_\alpha = \int_{\Omega_\alpha} \rho_\Omega(\mathbf{r}) \, d\mathbf{r} \quad \text{for } \alpha = 1, 2,$$

where ρ_Ω is the interior density (5). Thus the ratio of the total energies in each sub-domain is given by P_1/P_2. We note that the energy ratio between a pair of sub-domains is often a quantity of interest for high-frequency noise and vibration simulations in built-up structures since it gives a simple indicator for the extent to which the energy has spread between two given subdomains and correspondingly the strength of their coupling. Indeed, for SEA based models where a weak coupling assumption is implicit, then such ratios may be used to test the validity of the SEA model itself [9]. We also note that in SEA each subdomain (or subsystem) is modelled using only a single degree of freedom, that is the average vibrational or acoustic energy, and the detailed spatial resolution of the energy distribution given by the ray approach presented here is not available. Therefore, the energy ratios computed in this section may be used for a direct comparison between our ray based model and SEA, see for example Refs. [9,42] for an SEA analysis of the coupled domain configurations studied here.

In Fig. 7 we show the energy ratio in configuration *A* for four choices of $\boldsymbol{\sigma}$ with $\sigma_1 = \sigma_2$. For each choice of $\boldsymbol{\sigma}$ we refine the discretisation until we observe convergence in the energy ratio across the full range of frequencies considered. Here Δ indicates the minimal edge length present in each configuration and the average size of each boundary element for the spatial discretisation is quoted in the figure legend in terms of a fraction of Δ. In addition to the energy ratio plots, we also include plots of the logarithm of the interior density. All sub-plots in Fig. 7 use the same colour scale as indicated by the
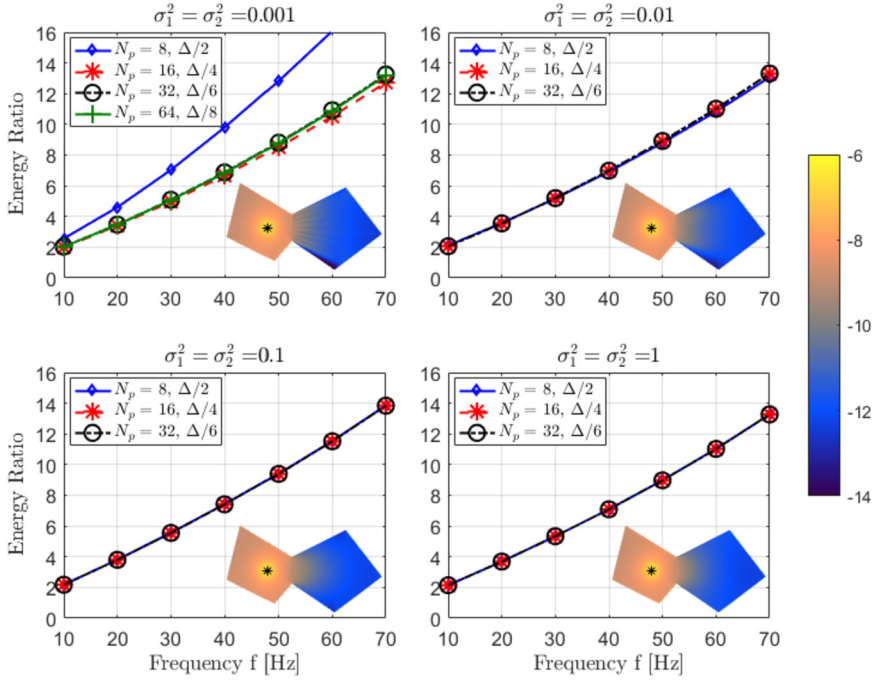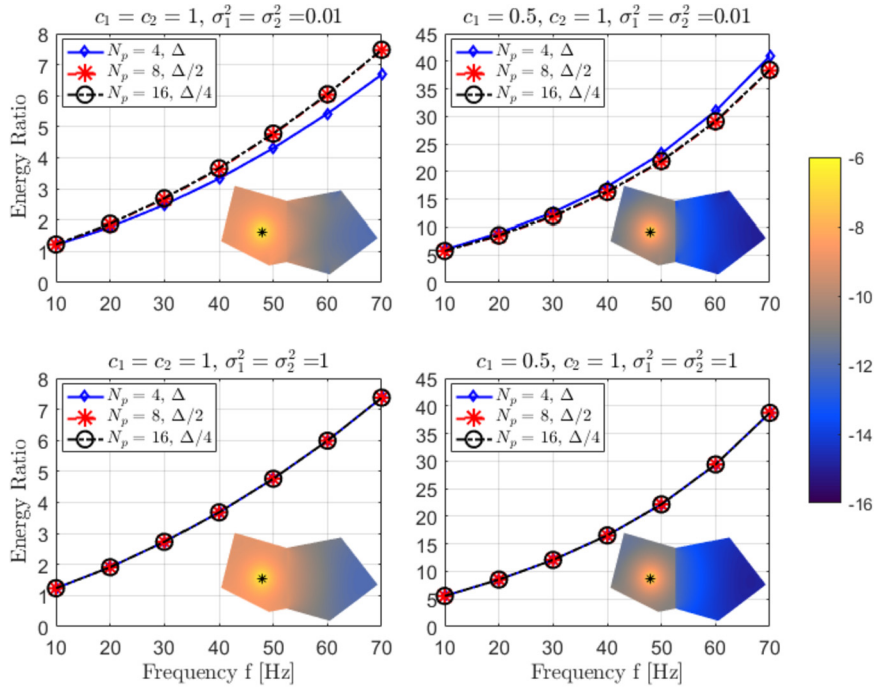
Fig. 7. Energy ratio P_1/P_2 in configuration *A* for different values of the frequency $f = \omega/(2\pi)$ and σ. Parameter values are the same in both sub-domains: $\Delta = 0.4$, $\eta = 0.01$, $c_1 = c_2 = 1$ and $\rho^f = \omega^{-2}$.
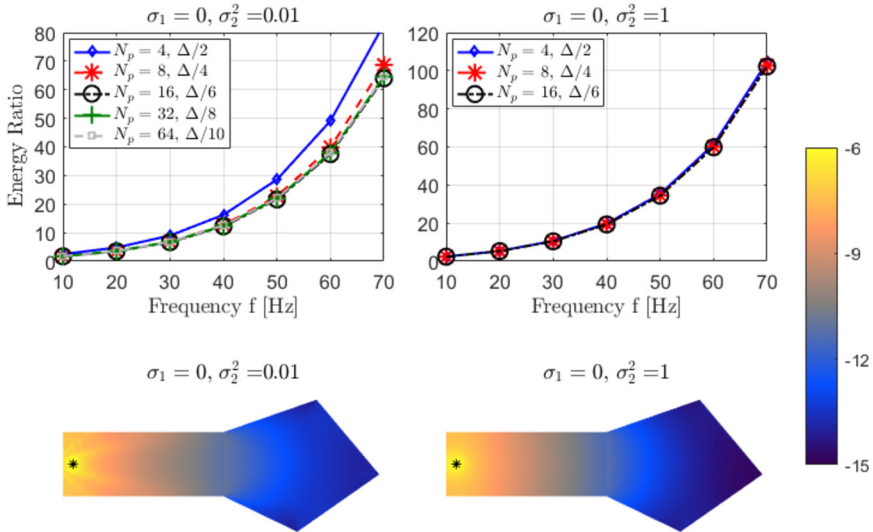
Fig. 8. Energy ratio P_1/P_2 in configuration *B* for different values of the frequency $f = \omega/(2\pi)$ and σ. Parameter values are the same in both sub-domains: $\Delta = 0.6$, $\eta = 0.01$, $c_1 = c_2 = 1$ and $\rho^f = \omega^{-2}$.

single colour bar on the right. The interior energy density plots are given for the case of $f = 70$ Hz only and for the most accurate discretisation choice listed in the figure legend.

For the numerical study of configuration *A* shown in Fig. 7 we choose $c_1 = c_2 = 1$, where c_α denotes the propagation speed in Ω_α for $\alpha = 1, 2$. Hence the transmission and reflection probabilities at the common edge are 1 and 0, respectively. However, for the larger values of σ considered, the interface acts as a ray scatterer due to uncertainties in both the position and the transmission angles. It is clear that in the simulations with $\sigma_1^2 = \sigma_2^2 = 0.001$, then the dynamics are very close to the deterministic case since we can identify a shadow zone in the lower part of Ω_2. This shadowing effect is caused by the relative positions of the source point and the common interface, together with high damping when $f = 70$ Hz. The shadow zone disappears when the values of σ_1 and σ_2 are increased, as shown in the lower plots of Fig. 7. We do not observe significant differences between the energy ratios computed with different values of σ. This is in contrast with what

Fig. 9. Energy ratio P_1/P_2 in configuration C for different values of the frequency $f = \omega/(2\pi)$ and σ. Parameter values: $\Delta = 0.2843$, $\eta = 0.01$ and $\rho_\alpha^f = (c_\alpha/\omega)^2$ for $\alpha = 1, 2$.

we observe for configuration B shown in Fig. 8, where the main difference is that Ω_1 now has a regular geometry with integrable ray dynamics [43].

In Fig. 8 we illustrate the numerical results for the energy ratios in configuration B. Once again we choose $c_1 = c_2 = 1$, but in this case we have chosen $\sigma_1 = 0$ to compare directly with the results of Fig. 3. Recall that in Fig. 3 we observed increased energy levels to the left and decreased energy levels to the right of the rectangular domain for larger σ_2 values. This is exactly the same result that we observe in Fig. 8, since the energy density in Ω_2 is lower in the right sub-plots than the left sub-plots. For the upper sub-plots this effect can be observed via the higher energy ratios given when $\sigma_2^2 = 1$ compared with $\sigma_2^2 = 0.01$.

For our final numerical study, shown in Fig. 9, we consider configuration C and two scenarios. In the left column we show the results of simulations with $c_1 = c_2 = 1$ and do not observe any significant qualitative differences compared to the results presented in Fig. 7. Note that the increased length of the common interface has led to the loss of the shadowing area shown in Fig. 7, and also (unsurprisingly) resulted in lower energy ratios. In the right column of Fig. 9 we take $c_1 = 0.5$ and $c_2 = 1$, which leads to transmission probabilities defined by [35]

$$\lambda_{\alpha, \beta}(\vartheta) = \frac{4 z_\alpha z_\beta \cos(\vartheta') \cos(\vartheta)}{(z_\alpha \cos(\vartheta) + z_\beta \cos(\vartheta'))^2}, \qquad (23)$$

for $\alpha, \beta = 1, 2$, $\alpha \neq \beta$. Here z_α is the specific acoustic impedance (i.e. the product of fluid density ρ^f and the propagation speed c_α) in Ω_α. Also, ϑ is the incoming angle of a ray arriving at the interface with respect to the normal vector (of the interface edge), and ϑ' is the refracted angle of the transmitted ray given via Snell's Law: $c_\beta \sin(\vartheta') = c_\alpha \sin(\vartheta)$. The discontinuous change of propagation speed has a significant effect on the energy ratio values and we can observe a significant reduction of the total energy in Ω_2. We note that we do not observe significant differences in the energy ratio values for different values of σ in either of the two scenarios.

6. Conclusions

We have presented a boundary integral model for the stochastic propagation of phase-space densities in both single and multi-domain problems. The collocation method has been applied in order to perform numerical experiments using piecewise constant basis functions in space and both Gaussian radial basis functions and Legendre polynomial basis functions in the direction variable. We have demonstrated the convergence properties of the collocation method and shown that they correspond to estimates that could be expected from the theory for second-kind integral equations. We have also studied convergence of the numerical scheme to an exact solution, which is available in the deterministic limit, and obtained better accuracy (with small fixed values of σ_2) than typically arises using a deterministic transfer operator based model. Gaussian

radial basis functions have been shown to give an advantageous level of accuracy with very low numbers of basis functions for direction dominated problems, but this may be at the sacrifice of greater accuracy for large numbers of basis functions due to poor conditioning. The extension of the method to multi-domains is considered, together with a demonstration of the numerical results for three different coupled domain configurations. In this case we observe a greater sensitivity to the parameters $\boldsymbol{\sigma}$ in the PDF (7) when the geometry is regular with integrable ray dynamics and a lower sensitivity for irregular domains with more complex ray dynamics. That is, a careful treatment of uncertainties in ray propagation models is most important when the problem under consideration includes a regular structure or acoustic cavity.

Acknowledgements

Appendix A. Convergence in $L^2(Q)$

In this appendix we discuss convergence theory for second-kind Fredholm integral equations in $L^2(Q)$, which can be applied directly to equation (3). In particular, we discuss the two assumptions required to apply Theorem 3.1.1 of Ref. [31], which tells us that the convergence rate for the collocation method solution to the integral equation (3) is the same as the convergence rate for the finite dimensional basis approximation of ρ.

Consider the boundary integral equation

$$(I - \mathcal{B})g = g_0, \tag{A.1}$$

posed on the boundary Q of a finite (phase-space) domain D, where $\mathcal{B} : L^2(Q) \to L^2(Q)$ is an integral operator of the form

$$(\mathcal{B}g)(X) := \int_Q b(X, Y)g(Y)\,\mathrm{d}Y,$$

I is the identity operator, and $g_0 \in L^2(Q)$ is a given boundary source term. The kernel function b is known and the goal is to solve (A.1) for $g \in L^2(Q)$.

In the case of the integral equation (3), the kernel function b is a weighted and truncated Gaussian and so is bounded. Unfortunately since

$$b(X, Y) = w(X, Y) f_{\boldsymbol{\sigma}}(X - \varphi(Y))$$

and the boundary map $\varphi(Y)$ undergoes a finite jump in the momentum component at corners of a polygon, then the function $b(X, Y)$ will be discontinuous as a function of Y. However, the following property of b is potentially beneficial for a convergence analysis in $L^2(Q)$.

Definition 1. The kernel function $b : Q \times Q \to \mathbb{C}$ is called a Hilbert–Schmidt kernel if

$$\int_Q \int_Q |b(X, Y)|^2 \,\mathrm{d}X\mathrm{d}Y < \infty.$$

A boundary integral operator $\mathcal{B}$ with a Hilbert–Schmidt kernel function is called a Hilbert–Schmidt operator.

It is easy to check that

$$0 \leq w(X, Y) f_{\boldsymbol{\sigma}}(X - \varphi(Y)) \leq (2\pi \sigma_1 \sigma_2 \psi_{\sigma_1}(X) \psi_{\sigma_2}(X))^{-1}$$

for all $X, Y \in Q = \Gamma \times (-c^{-1}, c^{-1})$ and so it is straightforward to generate a finite upper bound for the integral in Definition 1. An important property of Hilbert–Schmidt operators is that they are compact. If for $g \in L^2(Q)$ we additionally had that $(\mathcal{P}_{\boldsymbol{n}}g) \to g$ as $n, N \to \infty$ then we could invoke ([31], Lemma 3.1.2), which gives $\|\mathcal{B} - \mathcal{P}_{\boldsymbol{n}}\mathcal{B}\| = \|\mathcal{L}_{\boldsymbol{\sigma}} - \mathcal{P}_{\boldsymbol{n}}\mathcal{L}_{\boldsymbol{\sigma}}\| \to 0$ as n, $N \to \infty$. Unfortunately there exist $g \in L^2(Q)$ for which the projection (20) will not converge and we require more regularity than the Banach space $L^2(Q)$ provides. We therefore merely conjecture that $\|\mathcal{L}_{\boldsymbol{\sigma}} - \mathcal{P}_{\boldsymbol{n}}\mathcal{L}_{\boldsymbol{\sigma}}\| \to 0$ as $n, N \to \infty$ and note that the development of a more suitable function space framework for this analysis is an area for future work.

We now discuss the invertibility of the operator $(I - \mathcal{B})$. We note that if the $L^2(Q) \to L^2(Q)$ operator norm $\|\mathcal{B}\| < 1$ then the inverse is given by the Neumann series

$$(I - \mathcal{B})^{-1} = \sum_{j=0}^{\infty} \mathcal{B}^j$$

and is bounded by $\|(I - \mathcal{B})^{-1}\| \leq (1 - \|\mathcal{B}\|)^{-1}$. See for example [44], Theorem 2.14. It remains to justify that for the integral equation (3) we do indeed have $\|\mathcal{B}\| = \|\mathcal{L}_{\boldsymbol{\sigma}}\| < 1$. We make use of the property

$$\|\mathcal{L}_{\boldsymbol{\sigma}}\|^2 \leq \int\limits_{Q} \int\limits_{Q} (w(X, Y) f_{\boldsymbol{\sigma}}(X - \varphi(Y)))^2 \, \mathrm{d}Y \, \mathrm{d}X.$$

For single domain problems, the weight function w takes the form of a damping term $w(X, Y) = \exp(-\mu d(\varphi_s(t), t))$. Since $0 < f_{\boldsymbol{\sigma}}(X - \varphi(Y)) \leq (2\pi \sigma_1 \sigma_2 \psi_{\sigma_1}(X) \psi_{\sigma_2}(X))^{-1}$ then

$$\|\mathcal{L}_{\boldsymbol{\sigma}}\|^2 \leq \frac{1}{(2\pi \sigma_1 \sigma_2)^2} \int\limits_{Q} \frac{1}{\psi_{\sigma_1}(X)^2 \psi_{\sigma_2}(X)^2} \int\limits_{Q} e^{-2\mu d(\varphi_s(t), t)} \, \mathrm{d}Y \, \mathrm{d}X.$$

It is clear from their definition that the scaling functions ψ_{σ_1}, ψ_{σ_2} are bounded below by constants $0 < m_1, m_2 < 1$. We can therefore control the norm $\|\mathcal{L}_{\boldsymbol{\sigma}}\|$ using the decay rate parameter μ and hence $\|\mathcal{L}_{\boldsymbol{\sigma}}\| < 1$ can be assured for large enough μ.

References

[1] N. Atalla, F. Sgard, Finite Element and Boundary Methods in Structural Acoustics and Vibration, CRC Press, Florida, 2015.
[2] W. Desmet, P. Sas, D. Vandepitte, A comparison between an indirect Trefftz method and the finite element method for solving coupled vibroacoustic problems, J. Acoust. Soc. Am. 106 (1999) 2118.
[3] R. Lyon, R. DeJong, Theory and Application of Statistical Energy Analysis, Butterworth-Heinemann, Boston, 1995.
[4] A. Sestieri, A. Carcaterra, Vibroacoustic: the challenges of a mission impossible? Mech. Syst. Signal Process. 34 (2013) 1–18.
[5] T. Lafont, N. Totaro, A. Le Bot, Review of statistical energy analysis hypotheses in vibroacoustics, Proc. R. Soc. A 470 (2013).
[6] H. Kuttruff, Room Acoustics, 5th ed., Spon Press, UK, 2009.
[7] S. Fomel, J.A. Sethian, Fast-phase space computation of multiple arrivals, Proc. Natl. Acad. Sci. 99 (2002) 7329–7334.
[8] B. Engquist, O. Runborg, Computational high frequency wave propagation, Acta Numer. 12 (2003) 181–266.
[9] G. Tanner, Dynamical energy analysis – determining wave energy distributions in vibro-acoustical structures in the high-frequency regime, J. Sound Vib. 320 (2009) 1023–1038.
[10] D.J. Chappell, G. Tanner, Solving the stationary Liouville equation via a boundary element method, J. Comput. Phys. 234 (2013) 487–498.
[11] P. Cvitanović, R. Artuso, R. Mainieri, G. Tanner, G. Vattay, Chaos: Classical and Quantum, Niels Bohr Institute, Copenhagen, 2012, http://ChaosBook.org.
[12] J. Kajiya, The rendering equation, in: Proceedings of SIGGRAPH 1986, vol. 20, 1986, pp. 143–150.
[13] S. Siltanen, T. Lokki, S. Kiminki, L. Savioja, The room acoustic rendering equation, J. Acoust. Soc. Am. 122 (2007) 1624–1635.
[14] S. Ulam, Problems in Modern Mathematics, John Wiley and Sons, New York, 1964.
[15] C. Bose, R. Murray, The exact rate of approximation in Ulam's method, Discrete Contin. Dyn. Syst. 7 (2001) 219–235.
[16] M. Blank, G. Keller, C. Liverani, Ruelle–Perron–Frobenius spectrum for Anosov maps, Nonlinearity 15 (2002) 1905.
[17] O. Junge, P. Koltai, Discretization of the Frobenius–Perron operator using a sparse Haar tensor basis: the sparse Ulam method, SIAM J. Numer. Anal. 47 (2009) 3464–3485.
[18] J. Wormell, Spectral Galerkin methods for transfer operators in uniformly expanding dynamics, arXiv:1705.00431v2, 2017.
[19] H. Risken, The Fokker–Planck Equation, Springer, New York, 1996.
[20] V. Papadopoulos, I. Kalogeris, A Galerkin-based formulation of the probability density evolution method for general stochastic finite element systems, Comput. Mech. 57 (2016) 701–716.
[21] P. Cvitanović, C. Dettmann, R. Mainieri, G. Vattay, Trace formulas for stochastic evolution operators: weak noise perturbation theory, J. Stat. Phys. 93 (1998) 981–999.
[22] P. Cvitanović, C. Dettmann, R. Mainieri, G. Vattay, Trace formulas for stochastic evolution operators: smooth conjugation method, Nonlinearity 12 (1999) 939–953.
[23] P. Cvitanović, N. Søndergaard, G. Palla, G. Vattay, C. Dettmann, Spectrum of stochastic evolution operators: local matrix representation approach, Phys. Rev. E 60 (1999) 3936–3941.
[24] D. Lippolis, P. Cvitanović, How well can one resolve the state space of a chaotic map? Phys. Rev. Lett. 104 (2010) 014101.
[25] G. Palla, G. Vattay, A. Voros, N. Søndergaard, C. Dettmann, Noise corrections to stochastic trace formulas, Found. Phys. 31 (2001) 641–657.
[26] P. Cvitanović, D. Lippolis, Knowing When to Stop: How Noise Frees us from Determinism, American Institute of Physics, Melville, New York, 2012, pp. 88–126.
[27] J. Heninger, P. Cvitanović, D. Lippolis, Neighborhoods of periodic orbits and the stationary distribution of a noisy chaotic system, Phys. Rev. E 92 (2015) 062922.
[28] E. Bollt, P. Gora, A. Ostruszka, K. Zyczkowski, Basis Markov partitions and transition matrices for stochastic systems, SIAM J. Appl. Dyn. Syst. 7 (2008) 341–360.
[29] G. Froyland, O. Junge, P. Koltai, Estimating long term behavior of flows without trajectory integration: the infinitesimal generator approach, SIAM J. Numer. Anal. 51 (2013) 223–247.
[30] D.J. Chappell, G. Tanner, A boundary integral formalism for stochastic ray tracing in billiards, Chaos 24 (2014) 043147.
[31] K.E. Atkinson, The Numerical Solution of Integral Equations of the Second Kind, Cambridge University Press, UK, 1997.
[32] T. Hartmann, S. Morita, G. Tanner, D. Chappell, High frequency structure- and air-borne sound transmission for a tractor model using dynamical energy analysis, Wave Motion (2018), in press.
[33] D. Chappell, J. Bajars, G. Tanner, Modelling parametric uncertainties in vibroacoustics using a DEA approach, in: Proceedings of Inter-Noise 2017, Hong-Kong, 2017.
[34] J. Bajars, D.J. Chappell, T. Hartmann, G. Tanner, Improved approximation of phase-space densities on triangulated domains using discrete flow mapping with p-refinement, J. Sci. Comput. 72 (2017) 1290–1312.
[35] J. DeSanto, Scalar Wave Theory: Green's Functions and Applications, Springer, Berlin, 1992.
[36] J. Bajars, D.J. Chappell, Boundary integral models of stochastic ray propagation: discretisation via the collocation and Nyström methods, AIP Conf. Proc. 1836 (2017) 020054.
[37] L.N. Trefethen, Spectral Methods in MATLAB, SIAM, 2000.
[38] J.P. Boyd, Chebyshev and Fourier Spectral Methods, 2nd ed., Dover, Mineola, New York, 2000.
[39] G.E. Fasshauer, Meshfree Approximation Methods with MATLAB, World Scientific, Singapore, 2007.

[40] G.E. Fasshauer, J.G. Zhang, Preconditioning of Radial Basis Function Interpolation Systems via Accelerated Iterated Approximate Moving Least Squares Approximation, Springer, Netherlands, Dordrecht, 2009, pp. 57–75.
[41] J. Bajars, D.J. Chappell, N. Søndergaard, G. Tanner, Transport of phase space densities through tetrahedral meshes using discrete flow mapping, J. Comput. Phys. 328 (2017) 95–108.
[42] B. Mace, Statistical energy analysis: coupling loss factors, indirect coupling and system modes, J. Sound Vib. 279 (2005) 141–170.
[43] M. Gutzwiller, Chaos in Classical and Quantum Mechanics, Springer, New York, 1990.
[44] R. Kress, Linear Integral Equations, 3rd ed., Springer, New York, 2014.